PROCEEDINGS A

rspa.royalsocietypublishing.org

Research

Cite this article: Smith WR. 2016 Wave–structure interactions for the distensible tube wave energy converter. *Proc. R. Soc. A* **472**: 20160160.
http://dx.doi.org/10.1098/rspa.2016.0160

Received: 1 March 2016
Accepted: 1 July 2016

Subject Areas:
energy, applied mathematics, mathematical modelling

Keywords:
radiated wave, analytical solution, capture width, optimization

Author for correspondence:
Warren R. Smith
e-mail: w.smith@bham.ac.uk

Wave–structure interactions for the distensible tube wave energy converter

Warren R. Smith

School of Mathematics, University of Birmingham, Edgbaston, Birmingham B15 2TT, UK

WRS, 0000-0002-0778-3226

A comprehensive linear mathematical model is constructed to address the open problem of the radiated wave for the distensible tube wave energy converter. This device, full of sea water and located just below the surface of the sea, undergoes a complex interaction with the waves running along its length. The result is a bulge wave in the tube which, providing certain criteria are met, grows in amplitude and captures the wave energy through the power take-off mechanism. Successful optimization of the device means capturing the energy from a much larger width of the sea waves (capture width). To achieve this, the complex interaction between the incident gravity waves, radiated waves and bulge waves is investigated. The new results establish the dependence of the capture width on absorption of the incident wave, energy loss owing to work done on the tube, imperfect tuning and the radiated wave. The new results reveal also that the wave–structure interactions govern the amplitude, phase, attenuation and wavenumber of the transient bulge wave. These predictions compare well with experimental observations.

1. Introduction

The world is confronting a crisis in terms of increasing global energy requirements, the depletion of fossil fuels and the threats of global warming and climate change. Although the situation is daunting, it is not without hope. The vast unharnessed power of ocean waves offers the promise of a steady supply of renewable energy. The recently invented distensible tube wave energy converter (WEC) has the potential to achieve this promise (figure 1), but progress has been impeded by the limited scientific understanding of the radiated wave and wave–structure interactions.

THE ROYAL SOCIETY PUBLISHING

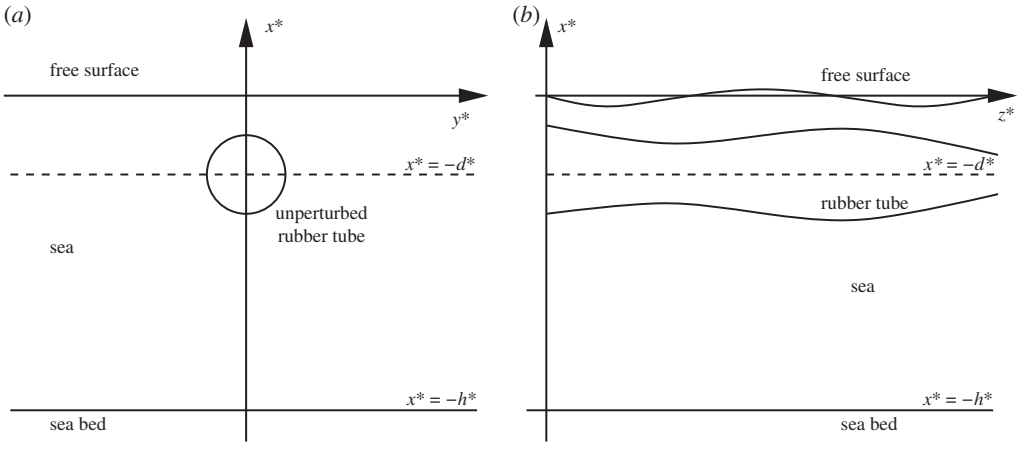

Figure 1. Two schematics of the distensible tube in the sea shows cross sections (*a*) from the front and (*b*) from the side, where the x^*-axis is vertical, the y^*-axis is horizontal and the z^*-axis is parallel to the axis of the unperturbed tube.

The analysis in the following focuses on the Anaconda, which is the first-patented distensible tube WEC [1] and is representative of the issues occurring in other WECs. It is based on the principle that pressure waves can propagate along a distensible tube [2,3]. These waves are usually referred to as bulge waves [1] owing to a local expansion in the tube that moves along its length. The device consists of a pressurized distensible tube filled with sea water and closed at the bow which is orientated parallel to the direction of gravity (or sea) waves. The pressure exerted by the gravity waves produces bulges and contractions in the tube that grow as they propagate. These bulges and contractions are accompanied by an oscillating flow inside the tube which is exploited by a power take-off (PTO) at the stern, the PTO being some mechanism capable of converting the kinetic energy into electricity. A number of factors limit the ability of this first-patented prototype to capture the energy in the gravity wave.

— The device may be optimized to respond well to some frequencies and wave speeds; however, ocean gravity waves are known to exhibit a range of frequencies and wave speeds with seasonal variations. The prototype will need to have a broad response to a range of frequencies.
— The efficient operation of the distensible tube requires the speed of the bulge wave to match the speed of the gravity wave in the sea, this being achieved by increasing the pressure inside the tube. Unfortunately, beyond a critical pressure, the tube becomes unstable and forms an undesirable aneurysm [4], an aneurysm being a large and permanent local expansion in the tube. Long tubes are capable of producing large bulge pressures that may attain this critical pressure. In order to postpone aneurysm formation in the tube, part of its circumference may be covered in longitudinal inextensible strips [5].
— The bulge wave may achieve a periodic steady state long before the PTO at the stern has been reached. In such circumstances, a large proportion of the tube would not contribute to energy capture.
— The dynamic response of a mechanical PTO would need to be matched to the bulge wave. Moreover, a mechanical PTO would suffer from high maintenance costs.

The subsequent patents of the distensible tube WEC device have included distributed PTO, in which power is extracted throughout the length of the distensible tube [4,6,7]. This limitation in the bulge pressure and amplitude will result in a substantial improvement in the energy conversion. Furthermore, these developments enable the tube to be protected against large bulge

amplitudes during a storm. This simple design will also benefit from low maintenance costs as there are no rotating parts or pumps.

A key issue for all these devices is that the basic scientific foundation has not been established for the distensible tube WEC. Even in the absence of the PTO, the physics has not been fully resolved in the peer-reviewed literature, the wave–structure interactions being the impediment. The mathematical models that have been constructed for the tube neglect the radiated wave. Following Lighthill [2], the standard approach has been to adopt a one-dimensional partially lumped model for the bulge pressure that describes small changes around the static inflation pressure. This simplified model has been successful in explaining how the bulge wave propagates in the tube in response to external pressure variations [3,4,8].

In this article, a self-consistent mathematical model is derived based on the principles of conservation of mass and momentum [9]. This comprehensive model incorporates the Laplace equation for the inviscid irrotational flow in the sea; the one-dimensional partially lumped model for the bulge in the tube that incorporates a Young–Laplace equation relating the bulge pressure and hoop stress; the appropriate hoop stress model for the distensible tube; the interface conditions on the tube relating fluid velocity, tube deformation and pressure; the boundary conditions at the free surface of the sea; the boundary condition at the sea bed and the lateral far-field boundary condition. In our model, the backward travelling bulge wave will be neglected and all other information propagates from bow to stern, which means that an additional model for the PTO at the stern is unnecessary. Furthermore, the changing frequency spectrum of ocean waves is replaced by a single incident frequency.

In British coastal waters, 40% of observed waves have amplitudes of 2 m or less with much longer wavelengths (up to a kilometre). It is standard practice to adopt a linear regular wave theory in this case based on the small parameter given by the ratio of these two length scales. The typical amplitude of the bulge wave is also less than 2 m. Therefore, the ratio of the amplitude of the bulge wave to the wavelength of the gravity waves is also a small parameter. Based on these ratios of length scales, a linear mathematical model is adopted in this article.

The energy capture of a WEC is measured in terms of capture width which is the ratio of the time-averaged absorbed power and the wave energy flux per unit crest length (often expressed in terms of diameters). Analytical predictions of capture width have been obtained when the governing equations are linearized and are analysed in the frequency domain. If a body with a vertical axis of symmetry oscillates in heave, then the maximum capture width is $\lambda/2\pi$, where λ is the incident wavelength. This theoretical result has proved very important [10–13]. More recent mathematical studies have provided the basis for optimizing the power absorption of submerged cylinder wave energy converters [14,15], the objective being to design a system which is effective over a range of wave periods. Our focus here is to obtain an analytical prediction for the capture width of the distensible tube WEC.

The role of an analytical solution to a linear mathematical model should be viewed in the appropriate context. Experimentalists are able to achieve more realistic wave conditions and numerical practitioners are able to incorporate more detailed nonlinear physics [16,17]. However, full scale trials and the use of computational approaches are all considerably more expensive than an analytical technique. Therefore, studies are limited to very restricted regions of parameter space, whereas analytical solutions are able to search large regions of parameter space for the optimal design. Analytical solutions should be used as a guide by device developers, experimentalists and numerical practitioners to ensure that expensive trials and tests are only conducted in the optimal region of parameter space.

High-quality experimental studies of the distensible tube WEC have taken place in the laboratory [3], typical data being shown in the third column of table 1. These experiments correspond to the first patent of these WECs with a PTO at the stern. We seek to use these results to obtain validation of our theoretical model. The most significant obstacle in making these comparisons is the bulge wave which is reflected from the PTO at the stern. In the scaled-down laboratory tests, this reflected wave will not rapidly decay, but will affect measurements throughout the length of the tube. The effect of the backward-travelling bulge wave is most

Table 1. Data for the series 2 experiments carried out at a scale of around 1 : 25, in [3] in the third column and for a prototype WEC in the fourth column. In the prototype, some values are taken from [4] and an incident wave period of 4 s is assumed.

symbol	definition	series 2 experiments in [3]	prototype WEC
h^*	water depth	1.87 m	100 m
r^*	pressurized tube radius	0.133 m	3.5 m
d^*	depth of tube	0.148 m	3.85 m
ρD	density multiplied by distensibility	9.8×10^{-2} m^{-2} s^2	2.5×10^{-2} m^{-2} s^2
ω_I	angular frequency of the incident wave	2.78 s^{-1}	1.57 s^{-1}
k_I	wavenumber of the incident wave	0.84 m^{-1}	0.25 m^{-1}
β^*	energy loss parameter	3.7×10^{-2} s	0.2 s
	tube length	6.8 m	300 m

pronounced near the bow; however, it is much less significant near the stern which allows us to obtain valuable comparisons. A secondary obstacle is the neglect of the nonlinear terms in our model, large amplitude bulge waves are beyond the scope of this study and, in any case, one would expect that a linear model to be appropriate for distributed PTO.

Section 2 formulates the mathematical model for the wave–structure interactions and scales the resulting system of equations. The periodic steady state is analysed in §3, approximate analytical expressions being obtained for the incident, radiated and bulge waves. Section 4 determines the transient bulge wave which attenuates as it propagates away from the bow. The energy capture of the WEC is deduced in §5, the mean power of the bulge wave and capture width being evaluated. Section 6 makes predictions of the capture width which go beyond previous experimental and theoretical studies. Finally, §7 gives a brief discussion of the results.

2. Formulation

(a) Governing equations

A Cartesian coordinate system (x^*, y^*, z^*) is adopted. We define the z^*-axis to be aligned with the axis of the unperturbed distensible tube and the y^*-axis to be horizontal. Gravity acts in the negative x^*-direction such that the free surface of the sea is located at $x^* = \eta^*(y^*, z^*, t^*)$, the axis of the tube at $x^* = -d^*$ and the sea bed at $x^* = -h^*$, where t^* is time. A schematic of the distensible tube in the sea is shown in figure 1.

We assume that the flow in the sea is inviscid and irrotational, viscous and rotational effects only being important in the wake of the WEC. The velocity potential, ϕ^*, is a function of three-dimensional space and time. The field equation for the velocity potential in the sea is

$$\frac{\partial^2 \phi^*}{\partial x^{*2}} + \frac{\partial^2 \phi^*}{\partial y^{*2}} + \frac{\partial^2 \phi^*}{\partial z^{*2}} = 0. \tag{2.1}$$

The pressure in the sea $p^*(x^*, y^*, z^*, t^*)$ is determined from the linearized Cauchy–Lagrange integral of the equations of motion

$$\frac{p^*}{\rho} = -\frac{\partial \phi^*}{\partial t^*} - g x^*, \tag{2.2}$$

where ρ is the density of sea water and g is the acceleration owing to gravity. The linearized dynamic and kinematic boundary conditions at the free surface of the sea are

$$\frac{\partial \phi^*}{\partial t^*} + g\eta^* = 0 \quad \text{and} \quad \frac{\partial \phi^*}{\partial x^*} = \frac{\partial \eta^*}{\partial t^*} \tag{2.3}$$

at $x^* = 0$ (unperturbed free surface). The zero normal velocity at the sea bed requires that

$$\frac{\partial \phi^*}{\partial x^*} = 0 \tag{2.4}$$

at $x^* = -h^*$. The far-field boundary condition assumes that the radiated wave decays rapidly and takes the form

$$\frac{\partial \phi^*}{\partial y^*} \to 0 \tag{2.5}$$

as $y^* \to \pm\infty$. The perturbed tube is of radius $R^*(z^*, t^*)$ with centre at $x^* = -d^*$ and $y^* = 0$, whereas the pressurized tube which is unperturbed by gravity waves is of radius r^* with the same centre. In fact, the axis of the tube translates in the vertical direction as the gravity wave passes. This translation is not of primary concern and is neglected in order to simplify this problem. At the surface of the tube, the continuity of the normal velocity requires that

$$\hat{\boldsymbol{n}} \cdot \left(\frac{\partial \phi^*}{\partial x^*}, \frac{\partial \phi^*}{\partial y^*}, \frac{\partial \phi^*}{\partial z^*} \right) = \frac{\partial R^*}{\partial t^*} \tag{2.6}$$

at $(x^* + d^*)^2 + y^{*2} = r^{*2}$ (unperturbed tube), where $\hat{\boldsymbol{n}}$ is the unit outward normal vector. The hoop strain, ϵ_{h}^*, is then given by

$$\epsilon_{\mathrm{h}}^* = \frac{R^* - r^*}{r^*}. \tag{2.7}$$

The distensible tube has a wall thickness H^* and Young's modulus E. The bulge pressure in the tube, p_{b}^*, is related to the hoop stress, σ_{h}^*, via the Young–Laplace equation $p_{\mathrm{b}}^* = \sigma_{\mathrm{h}}^* H^*/r^*$ owing to the thinness of the wall in comparison with its radius. Using the Kelvin–Voigt model, the hoop stress may be expressed as

$$\sigma_{\mathrm{h}}^* = E \left(\epsilon_{\mathrm{h}}^* + \beta^* \frac{\partial \epsilon_{\mathrm{h}}^*}{\partial t^*} \right),$$

where β^* corresponds to energy loss owing to work done on the tube [4]. We obtain

$$p_{\mathrm{b}}^* = \frac{EH^*}{r^*} \left(\epsilon_{\mathrm{h}}^* + \beta^* \frac{\partial \epsilon_{\mathrm{h}}^*}{\partial t^*} \right) = \frac{2}{D} \left(\epsilon_{\mathrm{h}}^* + \beta^* \frac{\partial \epsilon_{\mathrm{h}}^*}{\partial t^*} \right), \tag{2.8}$$

where D is the distensibility of the tube [2]. The total pressure inside the tube is given by $p_{\mathrm{b}}^* + p_{\mathrm{w}}^*$, where p_{w}^* is the pressure exerted by the sea on the tube. Following [2], the bulge pressure must also satisfy the following differential equation for the bulge wave

$$\frac{\partial^2 A}{\partial t^{*2}} = \frac{A_0}{\rho} \left(\frac{\partial^2 p_{\mathrm{b}}^*}{\partial z^{*2}} + \frac{\partial^2 p_{\mathrm{w}}^*}{\partial z^{*2}} \right),$$

where A is the cross-sectional area of the tube and A_0 is its unperturbed area. The cross-sectional area may be approximated in terms of the hoop strain by $A = A_0(1 + 2\epsilon_{\mathrm{h}}^*)$. Hence,

$$\frac{\partial^2 \epsilon_{\mathrm{h}}^*}{\partial t^{*2}} = \frac{1}{2\rho} \left(\frac{\partial^2 p_{\mathrm{b}}^*}{\partial z^{*2}} + \frac{\partial^2 p_{\mathrm{w}}^*}{\partial z^{*2}} \right). \tag{2.9}$$

The fluid in the tube is assumed to be stationary at the bow or $z^* = 0$, the axial pressure gradient being set to zero [3]. We have

$$\frac{\partial}{\partial z^*} (p_{\mathrm{b}}^* + p_{\mathrm{w}}^*) = 0 \tag{2.10}$$

at $z^* = 0$. A second boundary condition is required at the stern to determine the reflected wave. However, as the bulge wave is damped, the backward propagating wave will decay exponentially. We will neglect this wave and the associated boundary condition at the stern.

(b) Scaling

The model (2.1)–(2.10) corresponds to linear forced oscillatory waves in which the incident gravity wave acts as the forcing term. The solution of the mathematical problem consists of two parts (i) a periodic steady state that corresponds to the solution attained over large distances and (ii) the transient problem that describes the variation of the solution along the length of the tube. The periodic steady state has the same phase velocity as the incident wave, whereas the transient has a phase velocity associated with the wave–structure interactions. We assume that the incident gravity wave corresponds to the angular frequency ω_{I} and the corresponding wavenumber is k_{I} (discussed below). The governing equations and boundary conditions are transformed to dimensionless variables via

$$(x^*, y^*, z^*) = \frac{1}{k_{\mathrm{I}}}(x, y, z), \quad t^* = \frac{t}{\omega_{\mathrm{I}}}, \quad \phi^* = \frac{\epsilon\omega_{\mathrm{I}}}{k_{\mathrm{I}}^2}\phi, \quad \eta^* = \frac{\epsilon}{k_{\mathrm{I}}}\eta, \quad R^* = r^* + \frac{\epsilon}{k_{\mathrm{I}}}R,$$

$$(p^*, p_{\mathrm{b}}^*, p_{\mathrm{w}}^*) = \frac{\rho\epsilon\omega_{\mathrm{I}}^2}{k_{\mathrm{I}}^2}(p, p_{\mathrm{b}}, p_{\mathrm{w}}), \quad d^* = \frac{d}{k_{\mathrm{I}}}, \quad r^* = \frac{r}{k_{\mathrm{I}}}, \quad h^* = \frac{h}{k_{\mathrm{I}}},$$

where the small parameter $\epsilon \ll 1$ corresponds to small amplitude in comparison to wavelength. The dimensionless field equation for the velocity potential in the sea is given by

$$\frac{\partial^2\phi}{\partial x^2} + \frac{\partial^2\phi}{\partial y^2} + \frac{\partial^2\phi}{\partial z^2} = 0 \tag{2.11}$$

and the dimensionless pressure in the sea is determined by the equation

$$p = -\frac{\partial\phi}{\partial t} - \frac{\alpha}{\epsilon}x, \tag{2.12}$$

where $\alpha = gk_{\mathrm{I}}/\omega_{\mathrm{I}}^2$. The boundary conditions at the free surface of the sea become

$$\frac{\partial\phi}{\partial t} + \alpha\eta = 0 \quad \text{and} \quad \frac{\partial\phi}{\partial x} = \frac{\partial\eta}{\partial t} \tag{2.13}$$

at $x = 0$. The boundary condition at the sea bed and the far-field boundary conditions are given by

$$\frac{\partial\phi}{\partial x} = 0 \ \text{ at } x = -h \quad \text{and} \quad \frac{\partial\phi}{\partial y} \to 0 \ \text{ as } y \to \pm\infty, \tag{2.14}$$

respectively. The interface condition at the surface of the tube is

$$\hat{\boldsymbol{n}} \cdot \left(\frac{\partial\phi}{\partial x}, \frac{\partial\phi}{\partial y}, \frac{\partial\phi}{\partial z}\right) = \frac{\partial R}{\partial t} \tag{2.15}$$

at $(x + d)^2 + y^2 = r^2$. The dimensionless bulge pressure is related to the perturbations of the tube via

$$p_{\mathrm{b}} = c_0^2\Lambda\left(R + \beta\frac{\partial R}{\partial t}\right), \tag{2.16}$$

where $\beta = \beta^*\omega_{\mathrm{I}}$, $\Lambda = 2/r$ and $c_0^2 = k_{\mathrm{I}}^2/\rho D\omega_{\mathrm{I}}^2$. The differential equation for the bulge wave becomes

$$\Lambda\frac{\partial^2 R}{\partial t^2} = \frac{\partial^2}{\partial z^2}(p_{\mathrm{b}} + p_{\mathrm{w}}). \tag{2.17}$$

Finally, the boundary condition at the bow is given by

$$\frac{\partial}{\partial z}(p_{\mathrm{b}} + p_{\mathrm{w}}) = 0 \tag{2.18}$$

at $z = 0$.

3. Periodic steady state

(a) Incident wave

We now outline the leading-order solution for the incident wave (2.11)–(2.14) that corresponds to the standard progressive linear gravity wave. We have

$$\phi_{\mathrm{I}} = \eta_0 \frac{\cosh(x+h)\cos(z-t)}{\sinh(h)}, \quad \eta_{\mathrm{I}} = -\eta_0 \sin(z-t),$$

provided the dispersion relation

$$\alpha \tanh(h) = 1 \tag{3.1}$$

is satisfied. The incident angular frequency ω_{I} and wavenumber k_{I} have been chosen to satisfy (3.1). The corresponding pressure, p_{I}, may be deduced from the linearized Cauchy–Lagrange integral (2.12). The pressure difference across the tube drives its translational motion that we have already neglected. Any corresponding periodic variation of the incident or radiated wave on the surface of the tube is also neglected below.

(b) Radiated wave

This section considers the effects of the surrounding fluid (excluding the incident wave) which we expect to be dominated by the radiated wave. The wave diffracted from the bow will not be studied here. We formulate the problem for the radiated wave in terms of bipolar cylindrical coordinates in which we assume the sea bed to be in the far field. This transformation of the independent variables is adopted to simplify the domain: the equations for the radiated wave may be rewritten in a rectangular geometry. The drawback is that the equations become more complicated; nevertheless, these equations are simpler to solve in this geometry than the corresponding problem in Cartesian coordinates. We define

$$x = \frac{a\sinh(v)}{\cosh(v)-\cos(u)}, \quad y = \frac{a\sin(u)}{\cosh(v)-\cos(u)},$$

where $a = \sqrt{d^2 - r^2}$, $u \in [0, 2\pi)$ and $v \in [v_t, 0]$. The unperturbed tube is located at $v = v_t < 0$ in which $\cosh(v_t) = d/r$. The scale factors are

$$h_u = h_v = \frac{a}{\cosh(v)-\cos(u)}.$$

The field equation takes the form

$$\frac{1}{h_v^2}\left(\frac{\partial^2\phi}{\partial u^2} + \frac{\partial^2\phi}{\partial v^2}\right) + \frac{\partial^2\phi}{\partial z^2} = 0, \tag{3.2}$$

with the boundary conditions

$$\frac{1}{h_v}\frac{\partial\phi}{\partial v} = \frac{\partial R}{\partial t} \text{ at } v = v_t, \quad \frac{1}{h_v}\frac{\partial\phi}{\partial v} = \frac{\partial\eta}{\partial t} \text{ at } v = 0, \quad \frac{\partial\phi}{\partial t} + \alpha\eta = 0 \text{ at } v = 0 \tag{3.3}$$

and

$$\frac{\partial\phi}{\partial u}(0, v, z, t) = \frac{\partial\phi}{\partial u}(2\pi, v, z, t) = 0. \tag{3.4}$$

As our problem is autonomous in z and t, solutions are sought in the form of bulge waves propagating along the tube $R^{\mathrm{S}} = s_1\cos(z - t + \Psi_1)$, where $s_1 > 0$ is a dimensionless amplitude and Ψ_1 is the phase shift which are both to be determined. The superscript S indicates the periodic steady state. We seek a corresponding solution for the velocity potential

$\phi^S = s_1\phi_1(u,v)\sin(z-t+\Psi_1)$. The function ϕ_1 satisfies the boundary value problem

$$\frac{1}{h_v^2}\left(\frac{\partial^2\phi_1}{\partial u^2}+\frac{\partial^2\phi_1}{\partial v^2}\right)-\phi_1=0,$$

with

$$\frac{1}{h_v}\frac{\partial\phi_1}{\partial v}=1 \text{ at } v=v_t, \quad \frac{\alpha}{h_v}\frac{\partial\phi_1}{\partial v}=\phi_1 \text{ at } v=0, \quad \frac{\partial\phi_1}{\partial u}(0,v)=\frac{\partial\phi_1}{\partial u}(2\pi,v)=0.$$

We now seek a Fourier cosine expansion of the form

$$\phi_1(u,v)=\sum_{n=0}^{\infty} b_{1n}(v)\cos(nu).$$

The terms in $\cos(nu)$ are then equated to form an ordinary differential equation for b_{1n}. Apart from the first term of this expansion, the terms represent a periodic variation around the circumference of the tube. We now make the assumption that the dominant contribution to the uniform pressure exerted by the sea on the tube arises from the first term of this expansion. The expansion is truncated after the first term to yield $\phi_1 = b_{10}(v)$. We obtain the ordinary differential equation

$$\left(\frac{1}{2}\cosh(2v)+1\right)\frac{\mathrm{d}^2 b_{10}}{\mathrm{d}v^2}-a^2 b_{10}=0, \tag{3.5}$$

with the boundary conditions

$$\alpha\frac{\mathrm{d}b_{10}}{\mathrm{d}v}(0)=ab_{10}(0) \quad \text{and} \quad \cosh(v_t)\frac{\mathrm{d}b_{10}}{\mathrm{d}v}(v_t)=a. \tag{3.6}$$

We obtain a Taylor-series solution to the boundary value problem (3.5)–(3.6) about the ordinary point $v=0$ and within its radius of convergence of $\sqrt{\pi^2+\ln^2(2+\sqrt{3})}/2$

$$b_{10}=A_1\left(1+\frac{a^2}{3}v^2+\frac{a^2(a^2-2)}{54}v^4+\cdots\right)+B_1\left(v+\frac{a^2}{9}v^3+\frac{a^2(a^2-6)}{270}v^5+\cdots\right), \tag{3.7}$$

in which $B_1 = aA_1/\alpha$ and

$$A_1\left[\left(\frac{2a}{3}v_t+\frac{2a(a^2-2)}{27}v_t^3+\cdots\right)+\frac{1}{\alpha}\left(1+\frac{a^2}{3}v_t^2+\frac{a^2(a^2-6)}{54}v_t^4+\cdots\right)\right]=\frac{1}{\cosh(v_t)}.$$

We now choose to truncate this expansion at $\mathcal{O}(v^5)$. The accuracy of this truncated series solution (3.7) may be ascertained by comparing it with a numerical solution of the boundary value problem. The problem (3.5)–(3.6) is discretized using second-order finite differences and the tridiagonal matrix is inverted via the Thomas algorithm. Excellent agreement has been obtained between these two approximations for a number of parameter values.

(c) Bulge pressure

This section combines the results of the previous two subsections to determine the bulge wave. The pressure forcing term will be evaluated using equation (2.12). We neglect terms that vary with the azimuthal angle around the distensible tube to obtain the simplified expression

$$p_w^S=-\eta_0\frac{\cosh(h-d)\sin(z-t)}{\sinh(h)}+s_1 b_{10}(v_t)\cos(z-t+\Psi_1)+\frac{\alpha d}{\epsilon}.$$

Table 2. Solutions of equations (3.9) and the eight equations (4.4)–(4.6) using the data values from table 1.

	series 2 experiments	prototype
symbol	in [3]	WEC
s_1	1.3	0.34
Ψ_1	0.12	−0.85
a_0	1.0	1.0
a_1	5.0×10^{-2}	0.42
a_2	9.7×10^{-4}	5.1×10^{-2}
a_3	1.6×10^{-5}	7.3×10^{-3}
m	4.8×10^{-2}	9.6×10^{-2}
k_b	1.0	0.85
s_2	−1.3	−0.22
s_3	0.21	−0.20

Using (2.16), the bulge pressure may be written in the form

$$p_b^S = c_0^2 \Lambda s_1 [\cos(z - t + \Psi_1) + \beta \sin(z - t + \Psi_1)].$$

If we substitute these expressions for p_w^S and p_b^S into (2.17), then we find

$$s_1 P \sin(z - t + \Psi_1) - s_1 Q \cos(z - t + \Psi_1) = \Gamma \sin(z - t), \tag{3.8}$$

where

$$P = c_0^2 \Lambda \beta, \quad Q = \Lambda(1 - c_0^2) - b_{10}(v_t), \quad \Gamma = \eta_0 \frac{\cosh(h - d)}{\sinh(h)}.$$

Equation (3.8) determines the amplitude and phase shift as follows

$$s_1 = \frac{\Gamma}{(P^2 + Q^2)^{1/2}}, \quad \tan \Psi_1 = \frac{Q}{P}. \tag{3.9}$$

The term Γ, in the numerator of s_1, shows that the amplitude of the bulge wave has the expected linear dependence on the forcing from the incident wave. In the denominator of s_1, P corresponds to the energy loss owing to work done on the tube; the expression $\Lambda(1 - c_0^2)$ in Q is a measure of the damping owing to imperfect tuning of the bulge wave and the incident wave and $b_{10}(v_t)$ in Q is damping from the radiated wave. Solutions of equations (3.9) using the data values from table 1 are shown in table 2.

After some algebraic manipulation, we may rewrite the total pressure in the tube at periodic steady state as

$$p_b^S + p_w^S = P^S \cos(z - t + \Psi_1) + \frac{\alpha d}{\epsilon},$$

where $P^S = \Lambda s_1$. Figure 2*a* compares this prediction of amplitude P^S with the experimental results from figure 14 of Chaplin *et al.* [3] for a range of wave periods. The wave period of the incident wave is denoted by $T_I = 2\pi/\omega_I$ and $T_0 = 2.2$ s. The comparison is very good in the linear regime, but it fails near the resonance, nonlinear effects having been neglected in our mathematical model. Unfortunately, the backward-travelling wave also influences this comparison, as it reflects at the bow.

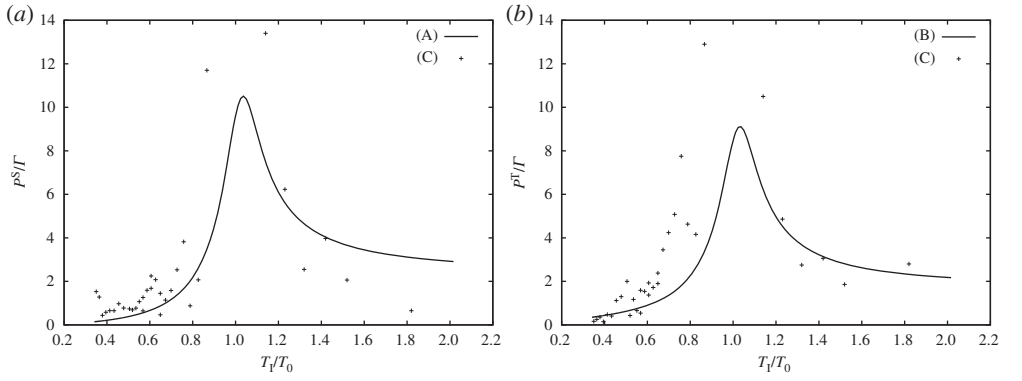

Figure 2. Amplitude of pressure in the tube plotted as a function of the relative wave period corresponding to the constituent with the (*a*) wavenumber of the incident wave and (*b*) wavenumber of the bulge wave: (A) amplitude of the pressure at periodic steady state, (B) amplitude of the transient pressure at the centre of the tube and (C) experimental results of Chaplin *et al.* [3]. The other data values are given in the third column of table 1.

4. Transient bulge wave

(a) Radiated wave

This section determines the transient radiated wave which varies along the length of the tube and complements our results at periodic steady state. As our problem is autonomous in z and t, solutions are now sought in the form of bulge waves which attenuate as they propagate along the tube

$$R^{\mathrm{T}} = \mathrm{e}^{-mz}[s_2 \cos(k_{\mathrm{b}} z - \omega_{\mathrm{b}} t) + s_3 \sin(k_{\mathrm{b}} z - \omega_{\mathrm{b}} t)],$$

where m is the dimensionless decay rate, $k_{\mathrm{b}} = k_{\mathrm{b}}^*/k_{\mathrm{I}}$ is the dimensionless wavenumber, $\omega_{\mathrm{b}} = \omega_B^*/\omega_{\mathrm{I}}$ is the dimensionless angular frequency, s_2 and s_3 are the dimensionless amplitudes. The superscript T indicates the transient. We now seek a corresponding solution of (3.2)–(3.4) of the form

$$\phi^{\mathrm{T}} = \omega_{\mathrm{b}}\, \mathrm{e}^{-mz}[s_2\phi_2(u,v)\sin(k_{\mathrm{b}} z - \omega_{\mathrm{b}} t) - s_3\phi_3(u,v)\cos(k_{\mathrm{b}} z - \omega_{\mathrm{b}} t)].$$

The functions ϕ_2 and ϕ_3 satisfy the coupled system of equations

$$s_2\bar{L}\phi_2 = s_3 2mk_{\mathrm{b}}\phi_3, \quad s_3\bar{L}\phi_3 = -s_2 2mk_{\mathrm{b}}\phi_2, \tag{4.1}$$

where the differential operator is given by

$$\bar{L} = \frac{1}{h_v^2}\left(\frac{\partial^2}{\partial u^2} + \frac{\partial^2}{\partial v^2}\right) + (m^2 - k_{\mathrm{b}}^2).$$

Equations in (4.1) may be combined to show that ϕ_2 satisfies the field equation

$$\bar{L}^2\phi_2 + 4m^2k_{\mathrm{b}}^2\phi_2 = 0.$$

The boundary conditions on ϕ_2 are

$$\frac{1}{h_v}\frac{\partial\phi_2}{\partial v} = 1, \quad \frac{1}{h_v}\frac{\partial(\bar{L}\phi_2)}{\partial v} = \frac{s_3}{s_2}2mk_{\mathrm{b}} \quad \text{at } v = v_t, \tag{4.2}$$

$$\frac{\alpha}{h_v}\frac{\partial\phi_2}{\partial v} = \omega_{\mathrm{b}}^2\phi_2, \quad \frac{\alpha}{h_v}\frac{\partial(\bar{L}\phi_2)}{\partial v} = \omega_{\mathrm{b}}^2(\bar{L}\phi_2) \quad \text{at } v = 0 \tag{4.3}$$

and

$$\frac{\partial\phi_2}{\partial u}(0,v) = \frac{\partial\phi_2}{\partial u}(2\pi,v) = \frac{\partial(\bar{L}\phi_2)}{\partial u}(0,v) = \frac{\partial(\bar{L}\phi_2)}{\partial u}(2\pi,v) = 0.$$

We seek a Fourier cosine expansion of the form

$$\phi_2(u,v)=\sum_{n=0}^{\infty} b_{2n}(v)\cos(nu).$$

As in the case of the periodic steady state, we make the assumption that the dominant contribution to the uniform pressure exerted by the sea on the tube arises from the first term of this expansion, all subsequent terms representing a periodic variation around the circumference of the tube. The expansion is truncated after the first term to yield $\phi_2=b_{20}(v)$. The linear operator $\bar{L}$ is approximated by L, where

$$L=\frac{1}{a^2}\left(\frac{1}{2}\cosh(2v)+1\right)\frac{\mathrm{d}^2}{\mathrm{d}v^2}+(m^2-k_\mathrm{b}^2).$$

We seek a Taylor-series expansion, about the ordinary point $v=0$ and within its radius of convergence of $\sqrt{\pi^2+\ln^2(2+\sqrt{3})}/2$, of the form

$$b_{20}=\sum_{n=0}^{7} a_n v^n,$$

where the coefficients a_n are to be determined. We also introduce the notation

$$Lb_{20}=\sum_{n=0}^{5}\bar{a}_n v^n$$

in order to simplify the subsequent algebra. The coefficients $\bar{a}_n$ are readily calculated to be

$$\bar{a}_0=\frac{3}{a^2}a_2+(m^2-k_\mathrm{b}^2)a_0, \qquad \bar{a}_1=\frac{9}{a^2}a_3+(m^2-k_\mathrm{b}^2)a_1,$$

$$\bar{a}_2=\frac{2}{a^2}(a_2+9a_4)+(m^2-k_\mathrm{b}^2)a_2, \qquad \bar{a}_3=\frac{6}{a^2}(a_3+5a_5)+(m^2-k_\mathrm{b}^2)a_3,$$

$$\bar{a}_4=\frac{1}{a^2}\left(\frac{2}{3}a_2+12a_4+45a_6\right)+(m^2-k_\mathrm{b}^2)a_4, \qquad \bar{a}_5=\frac{1}{a^2}(2a_3+20a_5+63a_7)+(m^2-k_\mathrm{b}^2)a_5.$$

We substitute these expansions into

$$L(Lb_{20})+4m^2k_\mathrm{b}^2b_{20}=0$$

and equate coefficients of powers of v to yield

$$\frac{54}{a^4}a_4=-\frac{6}{a^4}a_2-(m^2-k_\mathrm{b}^2)\left(\frac{3}{a^2}a_2+\bar{a}_0\right)-4m^2k_\mathrm{b}^2a_0,$$

$$\frac{270}{a^4}a_5=-\frac{54}{a^4}a_3-(m^2-k_\mathrm{b}^2)\left(\frac{9}{a^2}a_3+\bar{a}_1\right)-4m^2k_\mathrm{b}^2a_1,$$

$$\frac{810}{a^4}a_6=-\frac{12}{a^4}(a_2+18a_4)-\frac{2}{a^2}\bar{a}_2-(m^2-k_\mathrm{b}^2)\left(\frac{18}{a^2}a_4+\bar{a}_2\right)-4m^2k_\mathrm{b}^2a_2,$$

$$\frac{1890}{a^4}a_7=-\frac{60}{a^4}(a_3+10a_5)-\frac{6}{a^2}\bar{a}_3-(m^2-k_\mathrm{b}^2)\left(\frac{30}{a^2}a_5+\bar{a}_3\right)-4m^2k_\mathrm{b}^2a_3.$$

It remains to apply the boundary conditions. In order to evaluate a_0, a_1, a_2 and a_3, the following four equations may be deduced from (4.2) to (4.3)

$$\left.\begin{aligned}\cosh(v_t)\sum_{n=1}^{7}na_nv_t^{n-1}=a, \quad s_2\cosh(v_t)\sum_{n=1}^{5}n\bar{a}_nv_t^{n-1}=2mk_\mathrm{b}as_3\\ \text{and}\qquad \alpha a_1=a\omega_\mathrm{b}^2a_0, \qquad \alpha\bar{a}_1=a\omega_\mathrm{b}^2\bar{a}_0.\end{aligned}\right\} \tag{4.4}$$

It is not necessary to solve a similar problem for $\phi_3=b_{30}(v)$, as we may determine ϕ_3 using our solution for ϕ_2 and the first equation in (4.1).

(b) Bulge pressure

This section uses the results of the previous subsection to evaluate the transient bulge wave. The pressure forcing term will again be evaluated using equation (2.12). The pressure exerted on the tube by the wave radiated from the attenuated bulge wave is given by

$$p_{\mathrm{w}}^{\mathrm{T}} = \omega_{\mathrm{b}}^2\, \mathrm{e}^{-mz}[s_2 b_{20}(v_t)\cos(k_{\mathrm{b}}z - \omega_{\mathrm{b}}t) + s_3 b_{30}(v_t)\sin(k_{\mathrm{b}}z - \omega_{\mathrm{b}}t)].$$

Using (2.16), the bulge pressure may be written in the form

$$p_{\mathrm{b}}^{\mathrm{T}} = c_0^2 \Lambda\, \mathrm{e}^{-mz}[(s_2 - \omega_{\mathrm{b}}\beta s_3)\cos(k_{\mathrm{b}}z - \omega_{\mathrm{b}}t) + (s_3 + \omega_{\mathrm{b}}\beta s_2)\sin(k_{\mathrm{b}}z - \omega_{\mathrm{b}}t)].$$

If we substitute these expressions for $p_{\mathrm{w}}^{\mathrm{T}}$ and $p_{\mathrm{b}}^{\mathrm{T}}$ into (2.17) and equate coefficients of $\mathrm{e}^{-mz}\cos(k_{\mathrm{b}}z - \omega_{\mathrm{b}}t)$ and $\mathrm{e}^{-mz}\sin(k_{\mathrm{b}}z - \omega_{\mathrm{b}}t)$, then we obtain

$$\left.\begin{aligned} &[F - Jb_{20}(v_t)]s_2 + [G + Kb_{30}(v_t)]s_3 = 0 \\ \text{and}\quad &[-G - Kb_{20}(v_t)]s_2 + [F - Jb_{30}(v_t)]s_3 = 0, \end{aligned}\right\} \tag{4.5}$$

where $F = \Lambda[2mk_{\mathrm{b}}c_0^2\beta\omega_{\mathrm{b}} - c_0^2(m^2 - k_{\mathrm{b}}^2) - \omega_{\mathrm{b}}^2]$, $G = \Lambda[c_0^2\beta\omega_{\mathrm{b}}(m^2 - k_{\mathrm{b}}^2) + 2mk_{\mathrm{b}}c_0^2]$, $J = (m^2 - k_{\mathrm{b}}^2)\omega_{\mathrm{b}}^2$ and $K = 2mk_{\mathrm{b}}\omega_{\mathrm{b}}^2$.

(c) Bow boundary condition

The boundary condition at the bow (2.18) must be applied to the sum of the periodic steady state and the transient bulge wave. We have

$$\begin{aligned} p_{\mathrm{w}} = p_{\mathrm{w}}^{\mathrm{S}} + p_{\mathrm{w}}^{\mathrm{T}} &= -\Gamma\sin(z - t) + s_1 b_{10}(v_t)\cos(z - t + \Psi_1) + \frac{\alpha d}{\epsilon} \\ &\quad + \omega_{\mathrm{b}}^2\, \mathrm{e}^{-mz}[s_2 b_{20}(v_t)\cos(k_{\mathrm{b}}z - \omega_{\mathrm{b}}t) + s_3 b_{30}(v_t)\sin(k_{\mathrm{b}}z - \omega_{\mathrm{b}}t)], \\ p_{\mathrm{b}} = p_{\mathrm{b}}^{\mathrm{S}} + p_{\mathrm{b}}^{\mathrm{T}} &= c_0^2\Lambda s_1[\cos(z - t + \Psi_1) + \beta\sin(z - t + \Psi_1)] \\ &\quad + c_0^2\Lambda\, \mathrm{e}^{-mz}[(s_2 - \omega_{\mathrm{b}}\beta s_3)\cos(k_{\mathrm{b}}z - \omega_{\mathrm{b}}t) + (s_3 + \omega_{\mathrm{b}}\beta s_2)\sin(k_{\mathrm{b}}z - \omega_{\mathrm{b}}t)]. \end{aligned}$$

The boundary condition may be satisfied only if ω_{b} is very close to one. Henceforth, we assume $\omega_{\mathrm{b}} = 1$, the angular frequencies of the bulge and incident gravity waves being identical. In the experimental results of Chaplin *et al.* [3], the pressure was also found to be the sum of waves with differing wavenumbers, but all sharing the angular frequency of the incident wave. The coefficients of $\sin(t)$ and $\cos(t)$ are equated in (2.18) to yield

$$\begin{aligned} [M + k_{\mathrm{b}}b_{20}(v_t)]s_2 + [N + mb_{30}(v_t)]s_3 &= -\Lambda s_1\cos(\Psi_1), \\ [-N - mb_{20}(v_t)]s_2 + [M + k_{\mathrm{b}}b_{30}(v_t)]s_3 &= \Lambda s_1\sin(\Psi_1), \end{aligned}$$

where $M = c_0^2\Lambda(m\beta + k_{\mathrm{b}})$ and $N = c_0^2\Lambda(m - k_{\mathrm{b}}\beta)$. These equations may be rewritten in the form

$$\begin{pmatrix} s_2 \\ s_3 \end{pmatrix} = -\frac{\Lambda s_1}{\Delta}\begin{pmatrix} [M + k_{\mathrm{b}}b_{30}(v_t)]\cos(\Psi_1) + [N + mb_{30}(v_t)]\sin(\Psi_1) \\ [N + mb_{20}(v_t)]\cos(\Psi_1) - [M + k_{\mathrm{b}}b_{20}(v_t)]\sin(\Psi_1) \end{pmatrix}, \tag{4.6}$$

where

$$\Delta = [M + k_{\mathrm{b}}b_{20}(v_t)][M + k_{\mathrm{b}}b_{30}(v_t)] + [N + mb_{20}(v_t)][N + mb_{30}(v_t)].$$

Equations (4.4)–(4.6) determine the eight unknowns a_0, a_1, a_2, a_3, m, k_{b}, s_2 and s_3. This system of eight equations embodies the wave–structure interactions taking place along the distensible tube. The phase velocity of the bulge wave is not determined by the standard formula [2] for the distensibility in this coupled problem, but by the wave–structure interactions. The quantitative dependence of s_1 (on the energy loss owing to work done on the tube; the damping owing to imperfect tuning of the bulge wave and the incident wave; and damping from the radiated wave) carries forward to s_2 and s_3. The solutions of this system of eight equations are shown in table 2 for the data values given in table 1.

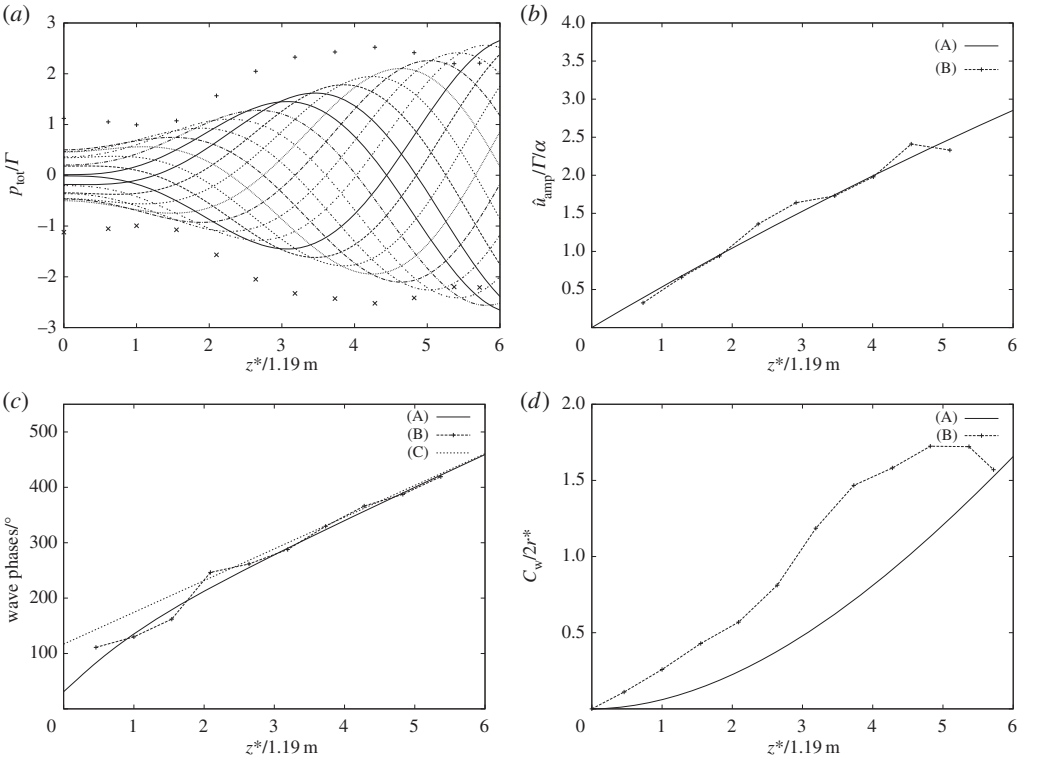

Figure 3. (*a*) The total pressure p_{tot} inside the tube normalized by the maximum pressure Γ outside the tube where lines denote analytical predictions, 16 snapshots over one period plotted over the length of the tube and points indicate the upper and lower envelopes of the corresponding experimental results in figure 11(c) of Chaplin *et al.* [3]. (*b*) The amplitude of the fluid velocity inside the tube $\hat{u}_{amp}$. The experimental results for the forward-travelling bulge wave in figure 11(e) of Chaplin *et al.* [3] have been shifted by a constant to pass through the origin. (*c*) The wave phases in degrees. (*d*) The capture width C_w in diameters. The experimental result at the stern represents the power which was converted at the PTO. The legends denote (A) analytical predictions for the bulge wave plotted over the length of the tube, (B) the experimental results for the bulge wave in figure 11 of Chaplin *et al.* [3] and (C) water wave phase shifted by 90°. The data values are given in the third column of table 1.

In order to gain experimental validation of our solution for the transient bulge wave, we seek a comparison with the experimental results in figure 14 of Chaplin *et al.* [3]. We compare the amplitude of the total transient pressure at the centre of the tube, P^T, for a range of wave periods with the corresponding experimental values in figure 2*b*. The agreement is very good in the linear regime, but fails in the nonlinear regime. Our mathematical model does not include nonlinear effects.

(d) Final solution

Our final solution is obtained by linear superposition of the solution for the periodic steady state and transient. Hence, the velocity potential $\phi = \phi_I + \phi^S + \phi^T$, where $\phi_I + \phi^S$ corresponds to the periodic steady state and ϕ^T to the transient. The form of the bulge wave propagating along the tube is the sum $R = R^S + R^T$. Similarly, the bulge pressure in the tube is given by $p_b = p_b^S + p_b^T$ and the pressure outside the tube by $p_w = p_w^S + p_w^T$.

Experimental validation of our final solution may be obtained by comparison with the results in figure 11(c) of Chaplin *et al.* [3]. The predicted total pressure $p_{tot} = p_b + p_w - \alpha d/\epsilon$ inside the tube is compared with these measurements in figure 3*a*. As expected (see the discussion in §1), the agreement is better towards the stern where our neglect of the backward-travelling wave is less

significant. The spatial oscillation in the upper and lower envelopes of the experimental results may be due to beating, whereas the predicted results have similar wavenumbers ($k_b = k_b^*/k_I = 1.0$) and identical frequencies in the incident and bulge waves so beating is not possible. It suggests that the incident and bulge waves contain different wavenumbers in the experiments of Chaplin *et al.* [3].

In figure 11(e) of Chaplin *et al.* [3], the amplitude of the fluid velocity inside the tube is plotted for the forward- and backward-travelling components of the bulge wave. The amplitude of the fluid velocity of the forward-travelling wave does not tend to zero at the bow, this non-zero value corresponding to the reflection of the backward-travelling wave. We wish to compare the growth rate of the forward-travelling bulge wave with our analysis, so this constant non-zero amplitude must be subtracted from the experimental results. Figure 3*b* compares these two growth rates, the agreement being excellent.

Further experimental validation may be obtained by comparison with the results in figure 11(f) of Chaplin *et al.* [3]. The wave phase for the overall solution for the bulge $R = R^S + R^T$ is compared with the measurements in figure 3*c*. The excellent quantitative agreement serves to validate both the structure of the bulge wave and the values obtained in the second column of table 2. The water wave minus 90 degrees is also plotted. As observed previously [3], the bulge wave after 3 m leads the water waves by approximately 90 degrees. However, during the first 3 m, the bulge wave may be seen to lead the water wave by significantly more than 90 degrees.

5. Energy capture

(a) Mean energy flux of the incident wave

In this section, we calculate the mean energy flux per unit crest length of the incident wave. The dimensional mean energy flux per unit crest length of the incident wave is

$$J_I^* = \frac{\omega_I}{2\pi}\int_{t^*=0}^{2\pi/\omega_I}\int_{x^*=-h^*}^{\eta^*} p_I^*\frac{\partial\phi_I^*}{\partial z^*}\,\mathrm{d}x^*\,\mathrm{d}t^*,$$

where $\phi_I^* = \epsilon\omega_I\phi_I/k_I^2$ and $p_I^* = \rho\epsilon\omega_I^2 p_I/k_I^2$. We non-dimensionalize and take the leading-order term on the right-hand side to obtain

$$J_I^* \sim \frac{1}{2\pi}\rho\frac{\epsilon^2\omega_I^3}{k_I^4}\int_{t=0}^{2\pi}\int_{x=-h}^{0} p_I\frac{\partial\phi_I}{\partial z}\,\mathrm{d}x\,\mathrm{d}t$$

as $\epsilon \to 0$. Using the linearized Cauchy–Lagrange integral (2.12) and periodicity of ϕ_I, our expression may be rewritten

$$J_I^* \sim \frac{1}{4}\rho\frac{\epsilon^2\omega_I^3}{k_I^4}\eta_0^2\frac{(\sinh(h)\cosh(h)+h)}{\sinh^2(h)}.$$

(b) Mean power of the bulge wave

We now evaluate the mean power of the bulge wave for the unsteady case. The dimensional mean power of the bulge wave is given by

$$P_b^* = \frac{\omega_I}{2\pi}\int_{t^*=0}^{2\pi/\omega_I}\int_{\bar{r}=0}^{R^*}(p_b^*+p_w^*)u^*2\pi\bar{r}\,\mathrm{d}\bar{r}\,\mathrm{d}t^*,$$

where $u^* = (\epsilon\omega_I/k_I)\hat{u}$ is the dimensional axial velocity of the water in the tube and $\bar{r}$ is the dimensional radial coordinate from the centre of the tube. As $p_b^* + p_w^*$ and u^* are independent

of $\bar{r}$, we may integrate to yield

$$P_{\mathrm{b}}^{*} = \frac{\omega_{\mathrm{I}}}{2} \int_{t^{*}=0}^{2\pi/\omega_{\mathrm{I}}} (p_{\mathrm{b}}^{*} + p_{\mathrm{w}}^{*}) u^{*} R^{*2} \, \mathrm{d}t^{*}.$$

We non-dimensionalize on the right-hand side to find that

$$P_{\mathrm{b}}^{*} \sim \frac{\rho}{2} \frac{\epsilon^{2} \omega_{\mathrm{I}}^{3} r^{*2}}{k_{\mathrm{I}}^{3}} I, \quad \text{where } I = \int_{t=0}^{2\pi} (p_{\mathrm{b}} + p_{\mathrm{w}}) \hat{u} \, \mathrm{d}t.$$

In §4, we determined that

$$p_{\mathrm{b}} + p_{\mathrm{w}} = \Lambda s_1 \cos(z - t + \Psi_1) + \frac{\alpha d}{\epsilon} + Y \mathrm{e}^{-mz} \cos(k_{\mathrm{b}} z - t) + Z \mathrm{e}^{-mz} \sin(k_{\mathrm{b}} z - t),$$

where

$$Y = s_2 b_{20}(v_t) + c_0^2 \Lambda (s_2 - \beta s_3), \quad Z = s_3 b_{30}(v_t) + c_0^2 \Lambda (s_3 + \beta s_2).$$

The differential equation (see [2])

$$\frac{\partial \hat{u}}{\partial t} = -\frac{\partial}{\partial z}(p_{\mathrm{b}} + p_{\mathrm{w}})$$

allows us to evaluate

$$\hat{u} = \Lambda s_1 \cos(z - t + \Psi_1) + \mathrm{e}^{-mz} \sin(k_{\mathrm{b}} z - t)[k_{\mathrm{b}} Z - mY] + \mathrm{e}^{-mz} \cos(k_{\mathrm{b}} z - t)[mZ + k_{\mathrm{b}} Y].$$

Hence,

$$\begin{aligned} I = {} & \Lambda^2 s_1^2 \pi + \Lambda s_1 \pi [(k_{\mathrm{b}} + 1)Z - mY] \mathrm{e}^{-mz} \sin((k_{\mathrm{b}} - 1)z - \psi_1) \\ & + \Lambda s_1 \pi [mZ + (k_{\mathrm{b}} + 1)Y] \mathrm{e}^{-mz} \cos((k_{\mathrm{b}} - 1)z - \psi_1) + k_{\mathrm{b}} [Y^2 + Z^2] \pi \, \mathrm{e}^{-2mz}. \end{aligned}$$

The first term in I is the value approached at the periodic steady state. An oscillatory behaviour is evident in the second and third terms in I when the transient and periodic steady state have different wavenumbers, this corresponding to beating.

(c) Capture width

The capture width of a wave energy converter is defined as the width of the wavefront from which all of the energy has been extracted. Optimization of the capture width is a key factor in the reduction of the cost of energy. We wish to derive an analytical approximation for the capture width of the distensible tube wave energy converter from the bow to the stern. The capture width, C_{w}, is approximated by

$$C_{\mathrm{w}} = \frac{P_{\mathrm{b}}^{*}}{J_{\mathrm{I}}^{*}} \sim \frac{2 r^{*2} k_{\mathrm{I}} I \sinh^2(h)}{\eta_0^2 (\sinh(h)\cosh(h) + h)}.$$

Figure 3*d* compares our prediction of the capture width over the length of the tube with the experimental measurements in figure 11(g) of Chaplin *et al.* [3], the agreement being reasonable. The capture width in the experiments will be increased by the reflection of the backward travelling bulge wave at the bow. Spatial oscillation is also evident in the experimental results, owing to the presence of a maximum, but does not appear in the analytical prediction, because the wavenumbers of the incident and bulge waves are similar ($k_{\mathrm{b}} = k_{\mathrm{b}}^{*}/k_{\mathrm{I}} = 1.0$). This spatial oscillation, which is associated with beating, is additional evidence that the incident and bulge waves contain different wavenumbers in the experiments of Chaplin *et al.* [3].

6. Results

(a) Small-scale predictions

We now use the data in the third column of table 1 to make predictions of the capture width which go beyond the experimental results published in Chaplin *et al.* [3]. Figure 4*a* shows the

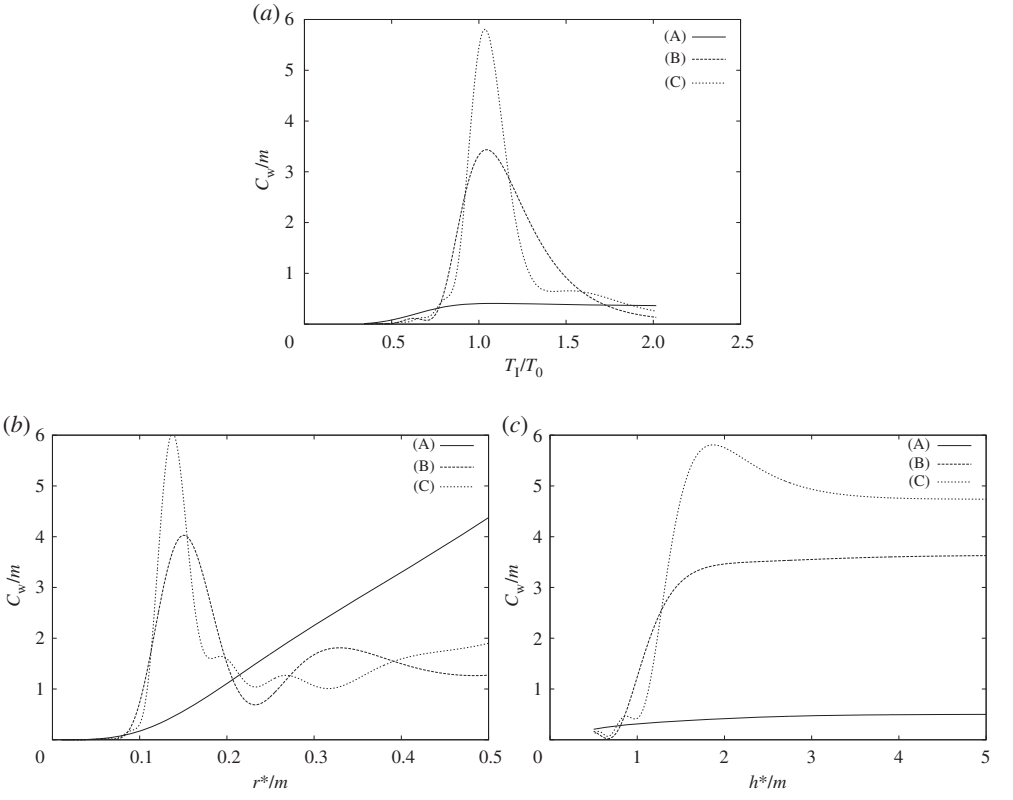

Figure 4. The capture width C_w plotted as functions of the (*a*) relative wave period, (*b*) pressurized tube radius and (*c*) water depth using an incident wavenumber of 0.84 m^{-1}, at three points along the length of the tube: (A) $z^* = 6.8$ m, (B) $z^* = 30$ m and (C) $z^* = 60$ m. The other data values are given in the third column of table 1.

variation of capture width with relative wave period for three locations along the tube 6.8, 30 and 60 m. At 6.8 m, the capture width exhibits a relatively flat and broad response to a range of wave periods. In contrast for the longer tubes of 30 and 60 m, there is a peak in the spectrum with an accompanying narrower response, the peak being most pronounced for the longest tube.

In figure 4*b*, the capture width is plotted as a function of pressurized tube radius at three locations along the tube. When varying the radius, we assume $d^* = \gamma r^*$ and $\gamma = 1.1$ to ensure that the tube remains just below the surface of the water. It is also important to recall that the distensibility is a linear function of radius (see (2.8)). At 6.8 m, the capture width increases monotonically as a function of radius; in other words, fatter and more expensive tubes will generate more energy. The capture width predictions at 30 and 60 m are much more complex: a global maximum for small radius is followed by oscillatory behaviour at larger radius. The wave–structure interactions are responsible for this series of local maxima. For longer tubes, fatter and more expensive devices will generate less electricity than suitably chosen thinner counterparts.

The variation of capture width with water depth at three locations along the tube is shown in figure 4*c*. At 6.8 m, the capture width increases by only a small amount with increasing depth. For the longer tubes of 30 and 60 m, there is a rapid increase in capture width as h^* increases from 1 to 1.5 m and, as expected, capture approaches a deep-water limit for depths greater than 4 m. For h^* below 1 m and between 1.5 m and 4 m, some maxima and minima are evident. In this case, changes in the dispersion relationship play an important role in addition to tuning, absorption and radiation effects. Indeed, for the longest tube, the global maximum in the capture width highlights the significance of water depth when mooring a distensible tube WEC in shallow water.

In order to further understand the optimal choice of pressurized tube radius and water depth, we consider a contour plot of capture width. Figure 5 shows a ridge of capture width in parameter

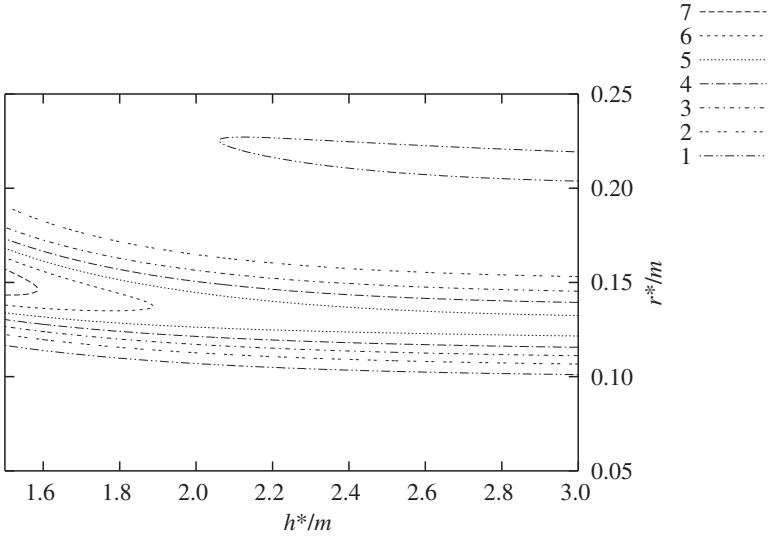

Figure 5. Contours of capture width at $z^* = 60$ m plotted as a function of water depth and pressurized tube radius. The capture width is in metres, and the incident wavenumber is 0.84 m^{-1}. The other data values are given in the third column of table 1.

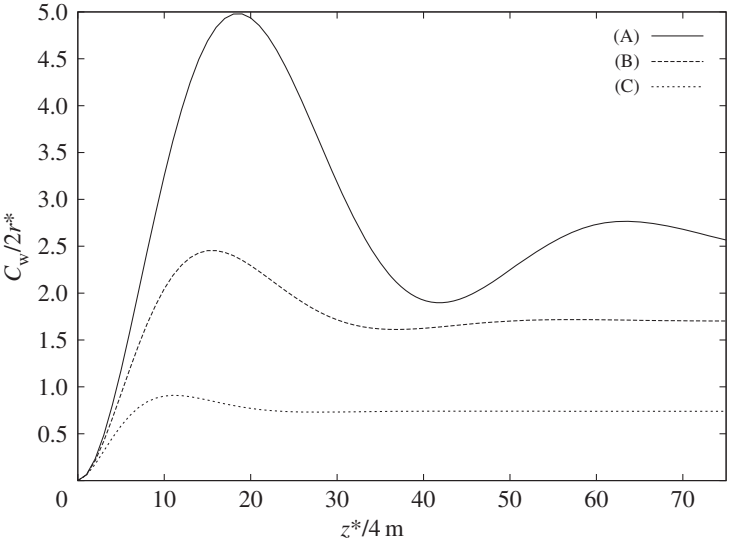

Figure 6. The analytical prediction of capture width C_w in diameters plotted over the length of a long tube with (A) $\beta^* = 0.1$ s, (B) $\beta^* = 0.2$ s and (C) $\beta^* = 0.4$ s. The other data values are given in the fourth column of table 1.

space. A WEC should appear along this ridge to achieve the most efficient energy generation. We note that the series 2 experiments in reference [3] have a remarkable agreement with the optimal choice of parameter values identified in figure 5.

(b) Industrial-scale predictions

This section predicts the performance of a prototype WEC described by the fourth column of table 1. Figure 6 shows that the capture width along the length of the tube for three values of the energy loss parameter. The oscillatory behaviour in figure 6 is due to beating, the ratio of the wavenumbers of the bulge and incident waves (k_b) being 0.85. An increase in the energy loss parameter damps the beating and reduces the mean values of capture width. Distributed PTO

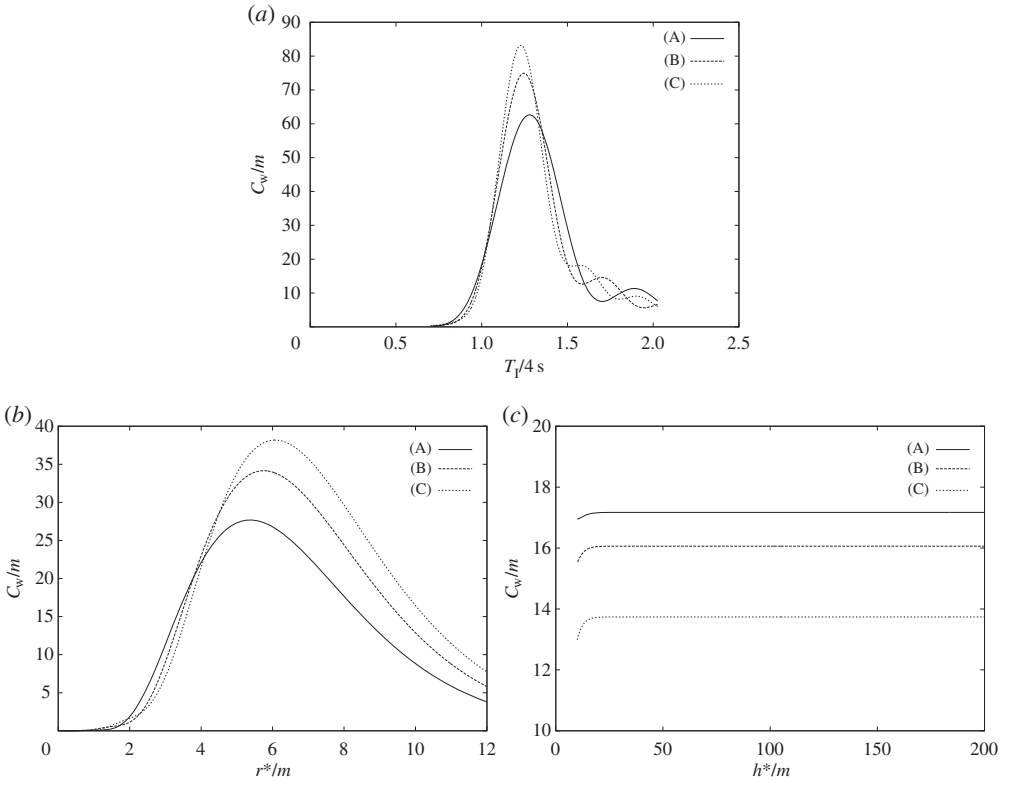

Figure 7. The capture width C_w plotted as functions of the (*a*) relative wave period, (*b*) pressurized tube radius and (*c*) water depth using an incident wavenumber of 0.25 m^{-1}, at three points along the length of the tube: (A) $z^* = 60$ m, (B) $z^* = 80$ m and (C) $z^* = 100$ m. The other data values are given in the fourth column of table 1.

would need to be carefully optimized in a distensible tube WEC in order to prevent the dramatic reduction in capture width seen in figure 6.

Figure 7 shows a similar behaviour to that already shown in figure 4 for the small-scale case. However, there are some notable differences: the capture widths are far greater; there is a broad response for a range of frequencies in figure 7*a*; beating may be seen in the oscillatory behaviour of figure 7*a*; and the capture width is almost independent of water depth in figure 7*c*. We also note that further along the length of the tube, the peak in capture width shifts to larger tube radius in figure 7*b*; the opposite trend was observed in figure 4*b*. In order to put these results into context, the maximum capture width for a distensible tube WEC of length 60 m in figure 7*a* is compared with the maximum capture width, of approximately 4 m, for a single heaving point absorber at this wavenumber. Therefore, this distensible tube WEC of length 60 m at resonance is equivalent to 20 heaving point absorbers at resonance.

7. Conclusion

A comprehensive mathematical model for the interactions of regular waves with a distensible tube has been introduced. The theory incorporates, for the first time, the effects of the radiated wave. Our approach differs from the approaches which have been previously reported. These existing approaches may be derived from our mathematical model by introducing engineering approximations to uncouple the system of equations. Our mathematical model requires the assumptions that the following phenomena may be neglected: (i) the vertical translations of the tube, (ii) nonlinear effects, (iii) the backward travelling bulge wave, and (iv) ocean wave spectra.

Assumption (iv) will need to be addressed in future work. Assumption (iii) is easily justified as the backward travelling wave will decay exponentially within a short distance of the stern for a full-scale prototype and will only be important in scaled-down laboratory tests. Assumptions (i) and (ii) may only be fully justified by comparison with experiment. Nonlinear effects have been shown to become important near resonance [8], but their significance would be limited by increased damping. Distributed PTO may well increase damping sufficiently to limit amplitudes to the linear regime studied here.

Our mathematical model and analytical solution techniques have been validated by numerous comparisons with the experiments in reference [3]. The superiority of our mathematical model may be seen in the comparison of figure 3(*c*) and figure 11(f) of Chaplin *et al.* [3]. Our model and the model in reference [3] agree that the bulge wave eventually leads the water waves by 90 degrees. However, the model in reference [3] predicts that the bulge wave leads the water wave by significantly less than 90 degrees during the initial stage, whereas our model predicts that the bulge wave leads the water waves by significantly more than 90 degrees. Our model predicts the experimental results quantitatively and captures the physical structure of the bulge wave for the first time.

Analytical techniques have been exploited to solve our coupled system of differential equations. One major advantage of these techniques is that parameter dependencies emerge in the course of the analysis which describes the underlying physics. The capture width has been found to vary linearly with

$$\frac{\cosh^2(k_{\mathrm{I}}(h^*-d^*))}{P^2+Q^2},$$

where

$$P=\frac{k_{\mathrm{I}}E\beta^*H^*}{\rho\omega_{\mathrm{I}}r^{*2}},\quad Q=\frac{2k_{\mathrm{I}}}{r^*\omega_{\mathrm{I}}^2}\left(\frac{\omega_{\mathrm{I}}^2}{k_{\mathrm{I}}^2}-\frac{1}{\rho D}\right)-b_{10}(v_t).$$

The numerator $\cosh^2(k_{\mathrm{I}}(h^*-d^*))$ represents absorption from the incident wave; P is the energy loss owing to work done on the tube; the first term in Q is damping owing to imperfect tuning of the incident and bulge waves, and the second term in Q is the damping owing to the radiated wave. In fact, the capture width at periodic steady state is given by

$$C_{\mathrm{w}}=\frac{8\pi\cosh^2(k_{\mathrm{I}}(h^*-d^*))}{k_{\mathrm{I}}(\sinh(k_{\mathrm{I}}h^*)\cosh(k_{\mathrm{I}}h^*)+k_{\mathrm{I}}h^*)(P^2+Q^2)}.$$

The role played by the pressurized tube radius is the most striking aspect of these formulae. As the tube radius increases, the damping owing to energy loss and owing to imperfect tuning decrease; however, provided that the tube remains just below the surface of the water ($d^*\approx r^*$), the increase in d^* will cause an exponential decrease in the absorption. Unfortunately, the radiation damping may not be expressed in such simple terms; nevertheless, tube radius has been identified as the most important design parameter in optimizing the energy capture.

The response of the capture width to a range of wave periods is evident by considering Q, the maximum in capture width being shifted from the tuned value of the distensibility by the radiated wave (as $|Q|\ll 1$). The maximum value of the capture width itself is then governed by P; that is, the energy loss owing to work done on the tube.

The wave–structure interactions taking place along the distensible tube are most evident in the solution of the transient problem. These interactions take the form of eight coupled nonlinear algebraic equations that determine the amplitude, phase, attenuation and wavenumber of the transient bulge wave. If the wavenumber of the incident wave differs from that of the transient bulge wave, then the spatial variation of the capture width is in the form of (potentially large) beating oscillations rather than monotonic growth. Large beating oscillations may have implications for the survivability of the device.

These analytical formulae will aid device developers as well as advance science in terms of improved understanding of the physics of WEC devices of this type. The main design parameters for a distensible tube have been identified as the radius and the length of the

device. Unfortunately, without optimization studies enabled by the mathematical model laid out in this article, fatter and longer tubes may be manufactured which have reduced energy capture. This conclusion is all the more pertinent with the capital costs for the production of the largest prototypes being prohibitively high. The introduction of distributed PTO will only further complicate the parameter dependence and optimization of these complex devices.

Distributed PTO may be incorporated into the mathematical model by replacing the Kelvin–Voigt constitutive equation for hoop stress (and possibly the equation for hoop strain) with an appropriate equation or system of equations. The remaining differential equations, interface and boundary conditions in the model will be unaffected by this modification. This has the significant advantage that the analytical solution obtained in §§3a,b and 4a will carry over to these devices and this analysis may be viewed as universal in this context. Therefore, our mathematical model may be modified to explore the feasibility for potential reductions in the cost of energy for different distributed PTO options.

Ethics. This work does not involve any human or animal data.

Data accessibility. This paper does not have any experimental data.

Funding. This work was not supported.

Competing interests. I have no competing interests.

Acknowledgements. This project has benefited from the constructive comments of three anonymous referees. The author is grateful to Prof. John Chaplin for providing the data from the experimental results in [3].

References

1. Farley FJM, Rainey RCT. 2006 *Distensible tube wave energy converter*. Patent no. GB 2434840 B.
2. Lighthill MJ. 1978 *Waves in fluids*. Cambridge, UK: Cambridge University Press.
3. Chaplin JR, Heller V, Farley FJM, Hearn GE, Rainey RCT. 2012 Laboratory testing the Anaconda. *Phil. Trans. R. Soc. A* **370**, 403–424. (doi:10.1098/rsta.2011.0256)
4. Farley FJM, Rainey RCT, Chaplin JR. 2012 Rubber tubes in the sea. *Phil. Trans. R. Soc. A* **370**, 381–402. (doi:10.1098/rsta.2011.0193)
5. Bucchi A, Hearn GE. 2013 Delay or removal of aneurysm formation in the Anaconda wave energy extraction device. *Renew. Energy* **55**, 104–119. (doi:10.1016/j.renene.2012.10.050)
6. Grey S, Borthwick A. 2014 Apparatus and method for extracting energy from fluid motion. US 8633608 B2.
7. Jean PF, Pollack J. 2012 *Wave energy converter*. Patent no. US 8120195 B2.
8. Mei CC. 2014 Nonlinear resonance in Anaconda. *J. Fluid Mech.* **750**, 507–517. (doi:10.1017/jfm.2014.277)
9. Ockendon JR, Howison SD, Lacey AA, Movchan AB. 1999 *Applied partial differential equations*. Oxford, UK: Oxford University Press.
10. Budal K, Falnes J. 1975 A resonant point absorber of ocean-wave power. *Nature* **256**, 478–479. (doi:10.1038/256478a0)
11. Evans DV. 1976 A theory for wave-power absorption by oscillating bodies. *J. Fluid Mech.* **77**, 1–25. (doi:10.1017/S0022112076001109)
12. Mei CC. 1976 Power extraction from water waves. *J. Ship Res.* **20**, 63–66.
13. Newman JN. 1976 The interaction of stationary vessels with regular waves. In *Proc.11th Symp. on Naval Hydrodynamics*, pp. 491–501. London, UK.
14. Crowley SH, Porter R, Evans DV. 2013 A submerged cylinder wave energy converter. *J. Fluid Mech.* **716**, 566–596. (doi:10.1017/jfm.2012.557)
15. Crowley SH, Porter R, Evans DV. 2014 A submerged cylinder wave energy converter with internal sloshing power take off. *Eur. J. Mech. B, Fluid* **47**, 108–123. (doi:10.1016/j.euromechflu.2014.03.008)
16. Chen LF, Zang J, Hillis AJ, Morgan GCJ, Plummer AR. 2014 Numerical investigation of wave–structure interaction using OpenFOAM. *Ocean Eng.* **88**, 91–109. (doi:10.1016/j.oceaneng.2014.06.003)
17. Westphalen J, Greaves DM, Williams CJK, Hunt-Raby AC, Zang J. 2012 Focused waves and wave–structure interaction in a numerical wave tank. *Ocean Eng.* **45**, 9–21. (doi:10.1016/j.oceaneng.2011.12.016)